Aerospace Science and Technology 144 (2024) 108825

Contents lists available at ScienceDirect

Aerospace Science and Technology

journal homepage: www.elsevier.com/locate/aescte

Powered turbofan effects on aircraft aerodynamics at high-lift: A study on the NASA CRM-HL

Andrea Magrini [a,*], Gokul Subbian [b], Rolf Radespiel [a], Ernesto Benini [b]

[a] Dipartimento di Ingegneria Industriale, Università Degli Studi di Padova, via Venezia 1, 35131, Padova, Italy
[b] Technische Universität Braunschweig, Hermann-Blenk-Str. 37, 38108 Braunschweig, Germany

ARTICLE INFO

Communicated by Damiano Casalino

Keywords:
NASA CRM-HL
High-lift aerodynamics
Installation effects
Ultra-high bypass ratio (UHBPR)
Body force model (BFM)
Propulsion system integration

ABSTRACT

High-lift operating conditions of aircraft are known to comprise a series of complex physical features, making the three-dimensional flow difficult to discern and analyse. In such scenario, the effect of underwing engine installation, especially in the case of large-diameter ultra-high bypass ratio turbofans, has been little investigated. In this paper, we present a numerical study on the NASA High-Lift Common Research Model aircraft with powered turbofan engines, focused on the effect of propulsion system integration. A validated Computational Fluid Dynamics model is first employed to analyse the aerodynamics along the wing polar, at an angle of attack up to 18°, close to near stall. The flow field on the suction side of aerodynamic surfaces is qualitatively similar to previous results obtained at lower Reynolds number for a throughflow nacelle, whereas on the pressure side a relevant distortion is present near the stall. The same case is simulated again by using a fully coupled Body Force Model fan stage representation, further inspecting the flow past the nacelle, the distribution of the propulsive forces, and the sensitivity of the fan working point to the operating incidence. The analysis reveals the complexity of the three-dimensional flow and the large azimuthal redistribution occurring on the nacelle, relative to an isolated configuration.

1. Introduction

High-lift conditions are naturally encountered during the take-off and landing phases of aircraft. Despite occupying a small fraction of the entire mission, especially for long-haul transport flights, they pose several challenges to airplane design and have a direct impact on the sizing, safety, and economics [1]. The high-lift flow past the wings is known to be characterised by a complex physics involving boundary layer transition, adverse pressure gradients, streamline curvature, vortical structures, and flow separation [2]. The capability of Computational Fluid Dynamics (CFD) solvers to predict this set of phenomena has been deeply assessed during the last decade in the AIAA High Lift Prediction Workshop (HLPW) series, where data from numerous participants were analysed to produce shared knowledge on best numerical practices, to enhance the computing capabilities, and to advance the understanding of the flow physics [3–6].

A major outcome from the HLPW series was the definition of public reference geometries and related wind tunnel data to be used as an experimental basis to determine the accuracy of CFD solutions, like the JAXA JSM [7] and the NASA CRM-HL [8]. Several authors investigated different numerical aspects related to Reynolds-Averaged Navier-Stokes (RANS) simulations of these aircraft models using various flow solvers. Zore et al. [9] presented the results of the HLPW-3 using Ansys Fluent. The authors employed κ-ω SST turbulence model and found that although consistent results could be obtained on hybrid unstructured grid refinement for the clean CRM-HL wing body, excessive flow separation developed for the JSM configuration with throughflow nacelle at stall conditions. Rudnik et al. [10] provided a similar report for the DLR solver TAU using RANS Spalart-Allmaras, confirming the trend of early separation at the wing root and at the wing tip due to slat tracks, and finding a limited influence of the grid resolution on the clean CRM-HL case. Duensing et al. [11] tested the influence of different RANS turbulence models and convergence methods using the structured curvilinear solver of NASA LAVA framework, before and near $C_{l,max}$. Ahmad et al. [12] described the HLPW-4 simulations conducted with FUN3D, including Wall-Modelled Large Eddy Simulations (WM-LES), finding that the latter agreed with RANS and experimental data of forces and pressure distribution at low angles of attack. Li et al. [13], Woeber et al.

* Corresponding author.
E-mail addresses: andrea.magrini@unipd.it (A. Magrini), g.subbian@tu-braunschweig.de (G. Subbian), r.radespiel@tu-bs.de (R. Radespiel), ernesto.benini@unipd.it (E. Benini).

https://doi.org/10.1016/j.ast.2023.108825
Received 13 October 2023; Received in revised form 29 November 2023; Accepted 10 December 2023
Available online 13 December 2023

[14], and Jones et al. [15] investigated the effect of unstructured mesh approaches and common guidelines modification on flow and aerodynamic coefficients. Ollivier-Gooch et al. [16] summarised the results of grid refinement for the HLPW-4, illustrating the large data scatter between the participants and the influence of different solution strategies, concluding that the use of very fine meshes is required to achieve grid convergence far from stall and highlighting the inability of RANS turbulence models to predict the near stall behaviour.

All the studies cited so far made use of wing body alone geometries or, in particular those conducted within the HLPW-4, wing body with a throughflow (TF) nacelle. This latter case is much more challenging, because of the complex interaction caused by vortical structures emanating from the wing/pylon joint and the nacelle chine, when present [17]. The current research is in fact focused on resolving the aerodynamics of high lift flows and identifying adequate methods to capture the near-stall behaviour, including automatic mesh adaption [18], high-order discretisation [19], Large Eddy Simulations [20]. Much less attention has been devoted to the problem of aeropropulsive interaction due to the installation of powered propulsors.

Propulsion system integration will play a major role in developing ultra-efficient and disruptive aircraft configurations and determining their real performance [21–23]. The installation effects of podded turbofans have been long studied in computational and numerical tests, with large attention in the last two decades to Ultra-High Bypass Ratio (UHBPR) turbofans [24]. However, they were mainly devoted to the cruise flight. At low-speed and high-incidence conditions, instead, little research has been published with regards to powered turbines. Most of the works with nozzle jet under a wing investigated noise generation from airframe interaction [25]. For instance, Jente et al. [26] conducted an experimental study on the noise emitted by an UHBPR turbofan with different flap settings. Angelino et al. [27] carried out a numerical research on the same subject, changing the engine position. Teruna et al. [28] employed a Lattice-Boltzmann method to study the noise emission with porous stators of a turbofan mounted on the NASA CRM-HL.

The effect of the underwing integration of a modern large-diameter compact nacelle at high lift on the aerodynamics and propulsive performance appears, instead, much less investigated in the literature. In the attempt of shading light on this topic, in this paper we provide a comprehensive analysis on the behaviour of an UHBPR turbofan installed on the NASA CRM-HL at take-off conditions with regards to engine/airframe interaction. The study focuses on two aspects, namely the aerodynamic phenomena and the flow field along the wing polar and the propulsive performance of the turbofan up to moderate incidence using a coupled fan model.

Yet with the known limitations of the adopted RANS formulation in accurately predicting the entire lift regime, the research provides a description of the aeropropulsive effect of a closely integrated UHBPR turbofan at full thrust and high incidence, highlighting the interaction with the wing body and the sensitivity of the turbomachinery to the operating conditions. Moreover, it complements a previously published work employing the same geometry installed on the high-speed version of the NASA CRM and investigated at cruise conditions [29], delivering a complete analysis on the upcoming class of aeronautic turbofans at two fundamental mission points.

The rest of the paper first presents the computational methodology and the propulsive metrics, and then illustrates the two aforementioned aspects, i.e., the angle of attack sweep and the coupled engine simulations, summarising in the end the main findings of the study.

2. Methods

2.1. Test case and operating conditions

The NASA High-Lift (HL) Common Research Model (CRM) used as aircraft body in the study was developed from the high-speed CRM and represents a modern wide body configuration typical of LONG-HAUL commercial airliners [8]. The HL version is equipped with high-lift leading edge and trailing edge devices with different deflection angles [30], including slat bracket, flap track fairings, and a throughflow nacelle. As mentioned in the introduction, this open geometry was used from the 3^{rd} AIAA HLPW, related to the verification and improvement of CFD capabilities in the low-speed, high-incidence regime, and has been tested in several wind tunnel campaigns, making a large set of valuable data publicly available [5,6].

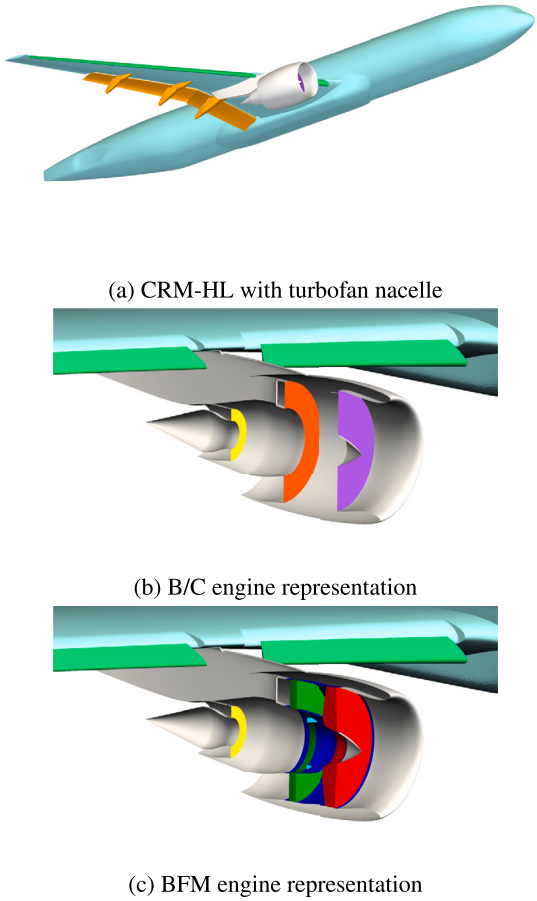

(a) CRM-HL with turbofan nacelle

(b) B/C engine representation

(c) BFM engine representation

Fig. 1. Illustration of the geometry and the two powered-on modelling strategies. (For interpretation of the colours in the figure(s), the reader is referred to the web version of this article.)

In the present research, the nominal landing configuration with no tail planes was employed for the validation of the computational model against experimental data and the assessment of grid resolution effects. The throughflow nacelle was then substituted with a turbofan engine simulated at powered-on conditions. The configuration is depicted in Fig. 1a. The propulsor model was conceived during the IVANHOE project and represents the new class of ultra-high bypass ratio engines to be adopted in commercial fleets in the next decade. The nacelle design process, based on successive refinements of a baseline geometry in a multi-level optimisation strategy aiming at maximising the net vehicle force at cruise under installation, is described in ref. [31–33]. The geometry was selected to ensure best cruise performance, with some off-design checks to verify the tolerability to low-speed high-incidence conditions. As such, the high-lift characteristics were not specifically optimised, but the non-axisymmetric scarfed and drooped intake parameters were selected based on data reported in the open literature, typically used to provide acceptable off-design performance [34,35].

For the simulation of the powered engine, two approaches were adopted, the first one based on the specification of boundary conditions at the interfaces between the gas turbine and the nacelle, the second based on a Body Force Model (BFM) of the fan stage. The former method

Table 1
Summary of simulated configurations and boundary conditions.

Case	M	Re	$\alpha°$	Flow solver	Engine model	Mesh level
Powered engine polar	0.26	39.6M	0–18	TAU	B/C	Fine
Coupled fan/airframe	0.26	39.6M	6, 12	Fluent	BFM	Medium

relied on a thermodynamic cycle model providing the flow status along different mission points and set as boundary conditions in the numerical simulation, thus here denoted as B/C. The corresponding domain boundaries are illustrated in Fig. 1b. The fan face (purple) was specified as a pressure outlet, whereas the fan outlet (orange) and the core outlet (yellow) were set as pressure inlet, with stagnation parameters imposed. The second method is presented apart in Sec. 2.2.3.

The computational model was developed based on AIAA HLPW guidelines [14,6] and was validated against experimental data for a scaled configuration with a throughflow nacelle. The numerical set-up was then replicated to study the CRM-HL with the UHBPR powered-on turbofan at take-off thrust rating, Mach number of 0.26, sea-level static pressure, static temperature T = ISA+15K and a range of angles of attack α from 6° to 18°, close to the wing $C_{L,max}$. The final task involved the coupled fan/airframe simulations of the same geometry but with the BFM of the fan stage, in place of the B/C representation. This last study was limited to $\alpha = 6°$ and 12°, to investigate the coupling between the fan stream and the airframe, and its impact on the propulsive performance. The detailed description of the computational approaches is given in the next paragraph, while Table 1 summarises the simulated cases.

2.2. Computational methods

2.2.1. Model validation

The validation of the numerical model was based on the experimental data available from the 4^{th} HLPW for a throughflow nacelle collected in the QinetiQ wind tunnel [36]. The flow solver employed was TAU [37] with Spalart-Allmaras turbulence closure (SA-neg version [38]), second order flux discretisation, and multigrid-accelerated steady state convergence. The grid employed was provided in the 4^{th} HLPW and corresponds to the hexahedral-tetrahedron dominant Level-D grid. The lift and drag polars are shown in Fig. 2, where the adherence of the computational prediction is good, with a slightly higher maximum C_L, due to the lower ability of steady RANS to accurately predict the flow field in this regime.

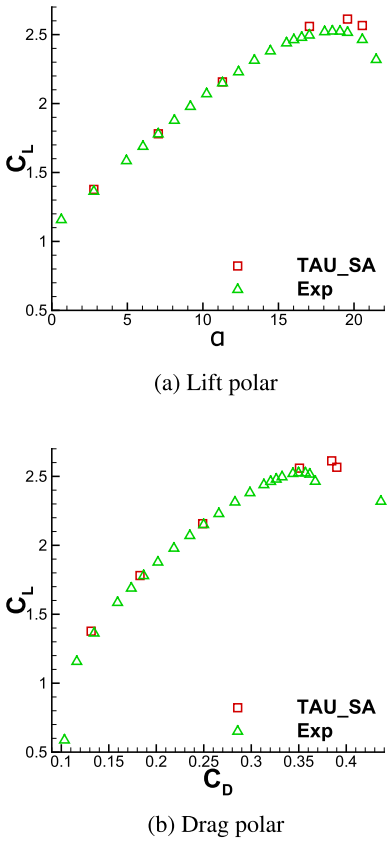

Fig. 2. Comparison of experimental and numerical data for throughflow nacelle tested in the QinetiQ wind tunnel for nominal landing configuration.

Local wing surface pressure distribution at $\alpha = 7.05°$ with different flap and slat deflections along the wing span is illustrated in Fig. 3, showing a general agreement with wind tunnel data. The wing suction peak is well matched for all configurations, with a small difference by around 0.20 C_p limited to belts A and B. The consistency with tunnel value is very good on the wing pressure side, and globally also on the suction side, especially for the nominal 40/37 configuration here employed, with local deviations up to 0.20 C_p occurring in belts D, G, and H, close to the trailing edge.

An additional comparison with experiments at near stall is given in Fig. 4, reporting the pressure coefficient at $\alpha = 17.05°$. Here, numerical results match wind tunnel data up to station F, whereas towards the wing tip an excessive suction side separation appears, causing the deviation from the experimental C_p. Such feature of RANS Spalart-Allmaras has been equally found in the HLPW-4 [6], and a similar result was obtained in [39] even for hybrid RANS/LES when using a very fine RANS grid. The stall regime is not specifically addressed in this study, and results obtained for the powered case at this condition are presented in Sec. 3.1 to give a qualitative comparison with similar numerical models employed for a throughflow nacelle.

2.2.2. Grid sensitivity for powered simulations

Grid sensitivity for powered simulations with B/C model in TAU solver was tested with three meshes compliant with the 4^{th} HLPW guidelines for levels A, B, and C, corresponding to coarse, medium, and fine. The unstructured grids generated had a wall-normal grown boundary layer region with the first cell height chosen to give $y^+ < 1$ in the medium level, based on Reynolds number of 39.6M at full-scale low-speed conditions. A hemispherical farfield boundary was placed 700 chord lengths away from the fuselage and freestream conditions were there specified. The wake and jet areas were refined with volumetric sources in order to cluster more cells in high gradient parts of the solution. Details of the meshes showing the surface elements distribution and the boundary layer expansion are illustrated in Fig. 5.

The sensitivity to the grid size was judged based on integral force values and local pressure distribution. Force coefficients at $\alpha = 6°$ are reported in Table 2, while the wing, slat, and flap surface pressure coefficient distribution is shown in Fig. 6, where η corresponds to the wing spanwise coordinate, starting from zero at the fuselage symmetry plane and being one at the wing tip. The first level was too coarse to properly resolve the flow, as indicated by the too low lift coefficient and the reduced suction on high-lift devices. The medium and fine mesh produced consistent results in terms of pressure distribution, with differences in the order of 5 force counts. Overall, local pressure distribution and global force coefficients indicated that results were converging towards the fine mesh, which was the one employed for powered simulations with TAU.

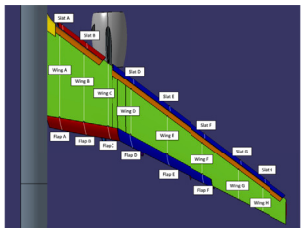

(a) Location of pressure probes belts

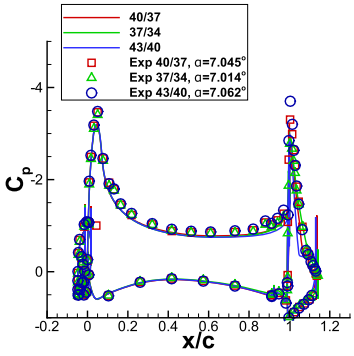

(b) Belt A

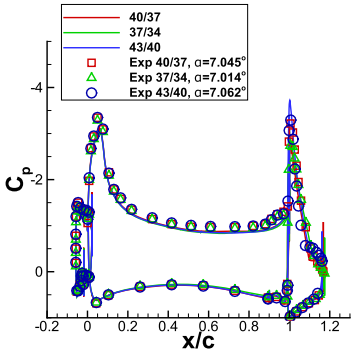

(c) Belt B

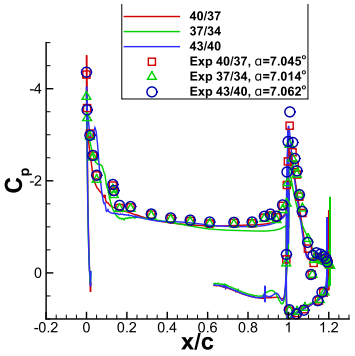

(d) Belt C

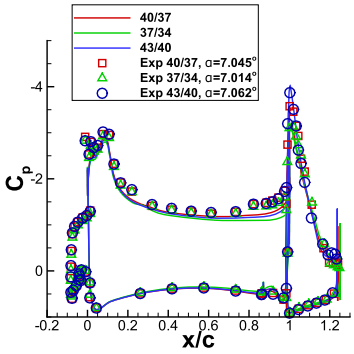

(e) Belt D

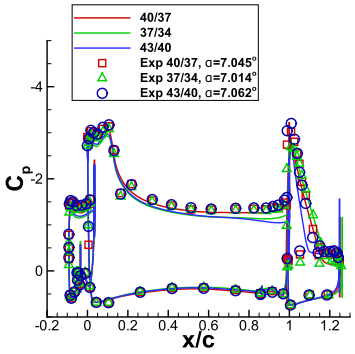

(f) Belt E

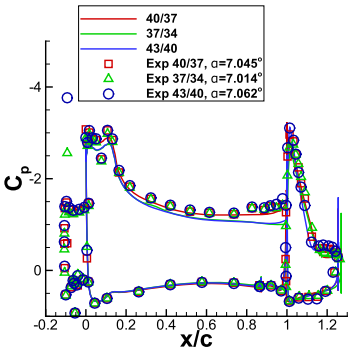

(g) Belt F

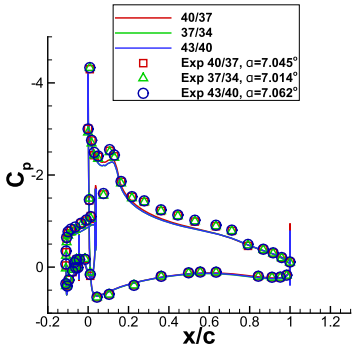

(h) Belt G

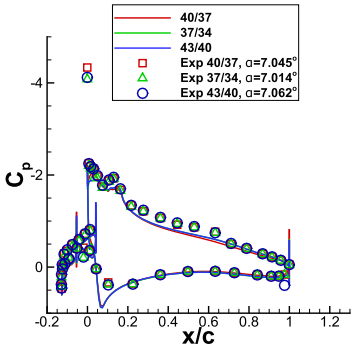

(i) Belt H

Fig. 3. Comparison of experimental and numerical wing pressure coefficient at different span sections and with three slat/flap deflections at $\alpha = 7.05°$, Re = 5.49M.

Table 2
Grid convergence study for B/C powered simulations with TAU at $\alpha = 6°$.

Mesh	No. Cells [M]	C_L	C_D	C_M
Coarse	20.8	1.7709	0.1796	-0.3918
Medium	56.9	1.7962	0.1748	-0.3868
Fine	128	1.7911	0.1753	-0.3863

2.2.3. *Fan stage body force modelling*

The coupled fan/airframe simulations were conducted with a body force model fan representation, reproducing the effect of the fan and Outlet Guide Vanes (OGV) blades through a force distribution appearing as a series of source terms in the Navier-Stokes equations. The model, derived from the Lift/Drag formulation of Thollet [40], is fully described in [41] and has been adopted in several studies, including the aforementioned investigation of the same nacelle geometry installed in the NASA High-Speed CRM at cruise conditions [29]. The validation of the BFM for the propulsor transonic fan and a discussion of its fidelity and limitations is reported in the same ref. [41,29]. Compared to 3D RANS CFD, the method applied to the current stage was shown to closely match the design point total pressure ratio and the mass flow rate over the speedline, with difference in stall pressure ratio of 0.5% at take-off thrust rating. Despite a lower ability to duplicate absolute efficiency values, with an under-prediction of around 2%, the BFM could accurately replicate the spanwise flow distribution and preserve a good accuracy in presence of inlet bulk swirl. The approach ensures the full coupling between the airframe flow and the fan stage. At high-incidence, the fan face distortion appears as an inhomogeneous swirl angle or total pressure distribution, forcing the fan to generate a non-uniform work input that in turn drives an upstream flow redistribution [42]. Moreover, in the take-off phase analysed, the fan nozzle was unchoked, making the discharge boundary condition of the fan sensitive to a change of the ambient pressure. Therefore, the adoption of a responsive fan model guarantees that, within its own accuracy, the change of the rotor operating point, the inlet and outlet distributions, and the bypass jet are reproduced by accounting for the physical interactions between the airframe and the engine. Such approach is thus more suited to investigate the sensitivity of the operating point to the external boundary conditions, as presented in Sec. 3.2.3. Instead, when the bulk effect of the powered propulsor is sought, like in Sec. 3.1 fo-

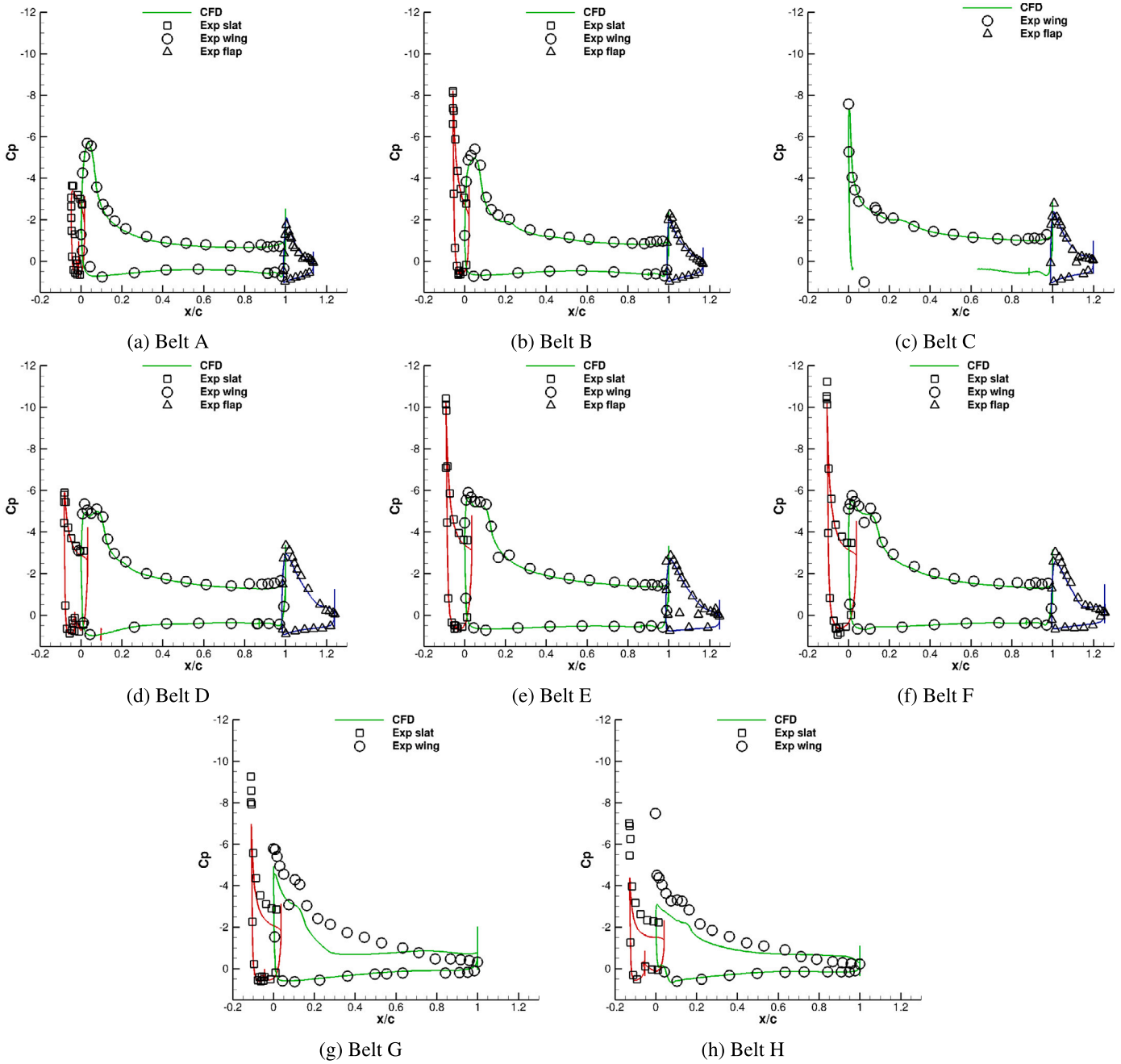

Fig. 4. Comparison of experimental and numerical wing pressure coefficient of nominal landing configuration at $\alpha = 17.05°$, Re = 5.49M.

cused on the external aerodynamics of the wings, the specification of constant boundary values on entry and exit planes provides a simpler representation matching globally the engine mass flow rate and the nozzle exit state.

The coupled simulations were executed using Ansys Fluent [43], where the BFM was implemented, keeping second-order fluxes discretisation and steady-state implicit time marching. The CRM-HL and turbofan geometries were the same of the TAU powered-on analysis. Due to the higher computational cost of the model, requiring also longer runs to achieve convergence due to the full coupling of internal and external flow, the grid employed was the medium one from the presented convergence study, with additional refinements in the inlet and exhaust areas to better resolve the interaction with the propulsor. In addition, the engine region across the bypass duct was now included in the computational domain, as illustrated in Fig. 1c, and inside the volume occupied by the fan and OGV rows the source terms of the BFM were activated. The number of cells was now 71.2M for the aircraft plus 6.5M elements in the BFM region, for a total of 77.7M cells. Since previous computations with the BFM had been carried out using the κ-ω SST turbulence closure [44], that was also adopted for its validation, and because the investigated angles of attack were far from the wing stall, in which the turbulence treatment has been reported to be more influential [45,16], κ-ω SST was used. Besides, previous preliminary investigations of powered nacelles we conducted with TAU, comparing κ-ω SST with Spalart-Allmaras, confirmed the substantial agreement between them in the linear range of the lift polar [46,47].

For a better assessment of the installation effects on the turbofan, the nacelle with pylon and BFM was also simulated in isolation at equal flight conditions. In this way, the influence of the wing and high lift devices on the fan response can be more clearly identified. The computational set up remained equal to the installed simulations, to ensure data consistency.

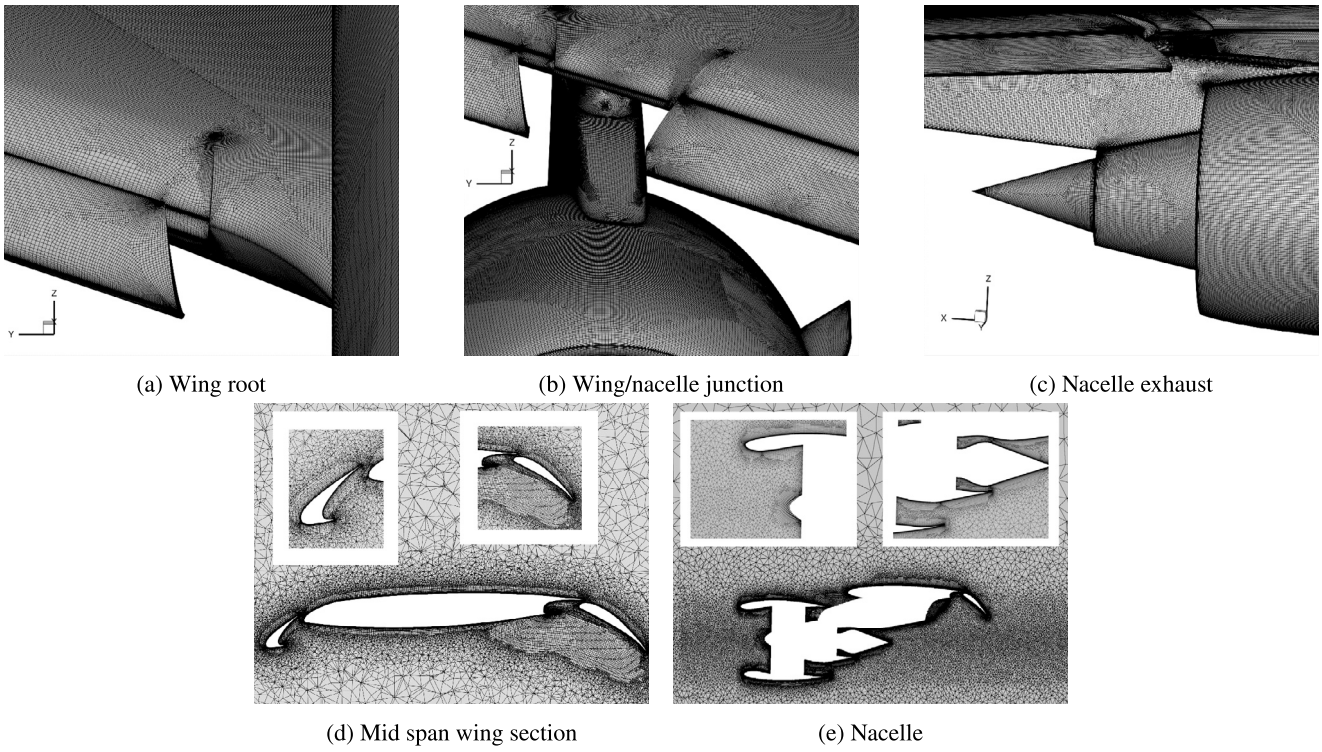

(a) Wing root (b) Wing/nacelle junction (c) Nacelle exhaust

(d) Mid span wing section (e) Nacelle

Fig. 5. Details of the grid employed for powered simulations. Fine level is shown.

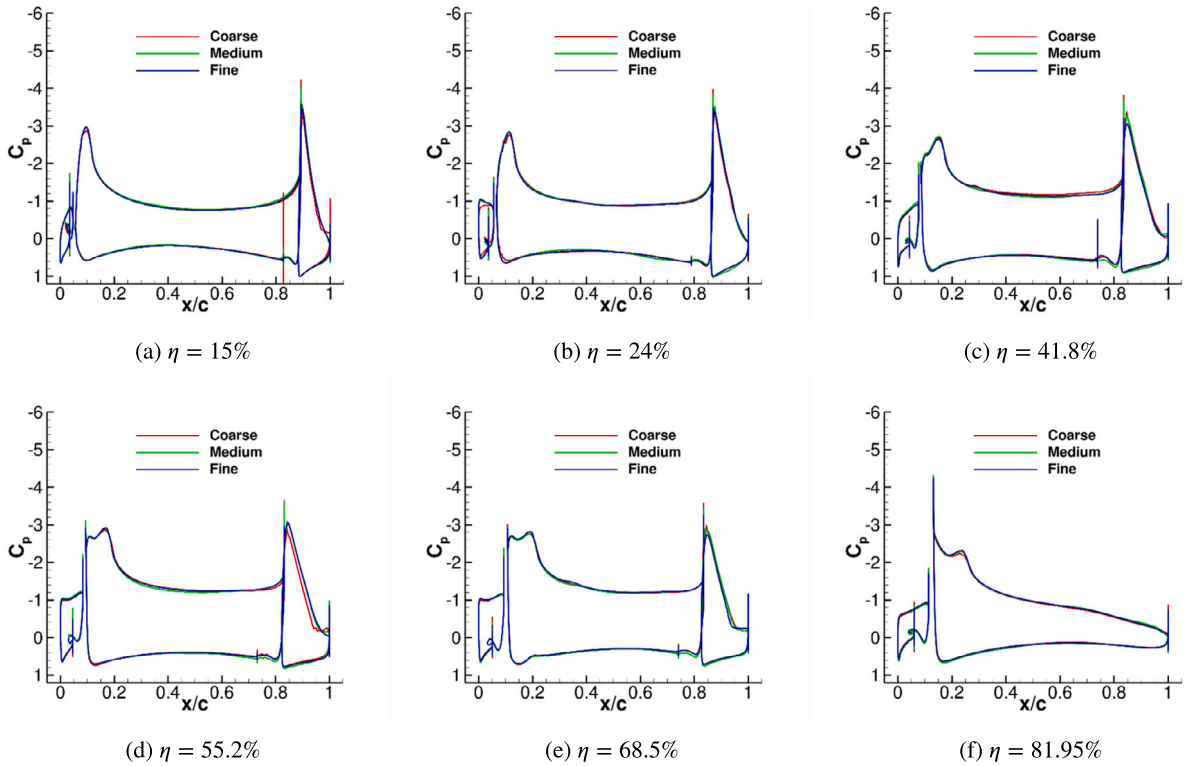

(a) $\eta = 15\%$ (b) $\eta = 24\%$ (c) $\eta = 41.8\%$

(d) $\eta = 55.2\%$ (e) $\eta = 68.5\%$ (f) $\eta = 81.95\%$

Fig. 6. Pressure coefficient variation with grid size for B/C powered simulation with TAU at $\alpha = 6°$.

2.3. Thrust/drag bookkeeping

The propulsive forces acting on the airframe and engine were monitored according to a Thrust/Drag Bookkeeping (TDB) procedure, based on a conventional decomposition into thrust and drag domain. The generic force on a solid surface of normal $\hat{n}$

$$\vec{f} = \int_A [(p - p_\infty)\hat{n} + \bar{\bar{\tau}}\hat{n}]\mathrm{dA} \tag{1}$$

is projected along the direction of interest $\hat{a}$ to give:

$$\phi, \theta = \vec{f} \cdot \hat{a} \tag{2}$$

Table 3
Definitions of the aggregated forces used in thrust/drag bookkeeping.

Metric	Symbol	Definition	Meaning
Total drag	D	$\phi_{nac} + \phi_{wing} + \phi_{slat} + \phi_{flap} + \phi_{fuselage} + \phi_{pylon}$	Drag force on airframe and nacelle cowl
Intrinsic Net Thrust	INT	$FG_{17} + FG_7 + FG_2$	Net gauge force change across the engine
Gross Propulsive Thrust	GPT	$GPT = FG_{17} + FG_7 + \theta_{fn} + \theta_{cn} + \theta_{cc} + \theta_{plug} + \theta_{pylon}$	Thrust force acting on the exhaust
Net Propulsive Thrust	NPT	$GPT + \theta_{int} + \theta_{sp} + \phi_{nac}$	Total net thrust delivered by the engine
Net Vehicle Thrust	NVT	$NPT + D$	Net force acting on the whole vehicle

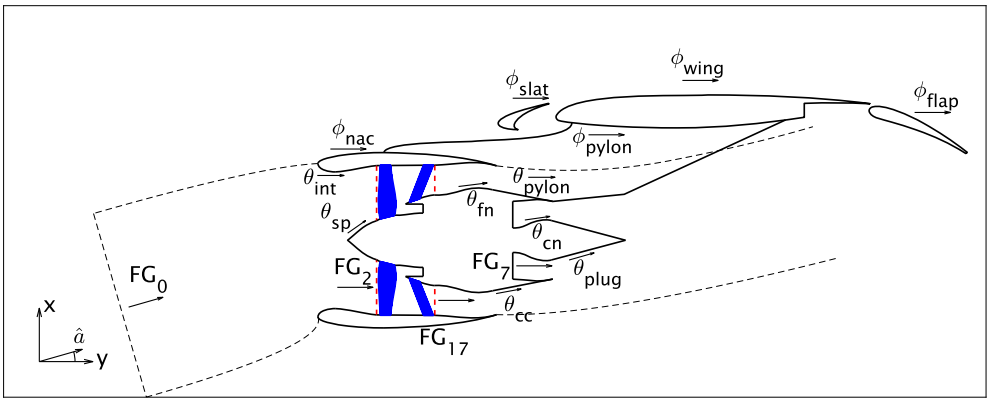

Fig. 7. Schematic of the thrust/drag bookkeeping forces acting on the airframe and nacelle.

When $\hat{a} = \vec{V}_\infty / ||\vec{V}_\infty||$, a positive value indicates the force component is acting as a drag and a negative value as a thrust. ϕ refers to those parts belonging to the drag domain, and θ to those on the thrust domain (Fig. 7).

On throughflow boundaries, the force is given by:

$$\overrightarrow{FG} = \int_A [(p - p_\infty)\hat{n} + \rho \vec{V}\left(\vec{V} \cdot \hat{n}\right)] dA = \int_A \overrightarrow{fg} dA \tag{3}$$

which is called the gauge stream force. By assembling the forces, the definitions given in Table 3 are employed. The total drag D includes the wing, fuselage, high-lift devices with their supporting parts, nacelle external cowl and pylon. The engine Gross Propulsive Thrust (GPT) measures the force acting on the exhaust. The Net Propulsive Thrust (NPT) is the net force delivered by the propulsor to the wing body. Finally, the Net Vehicle Thrust (NVT) is the algebraic sum of total drag and NPT and represents the net force acting on the whole vehicle. Note that arithmetic sum is used since the sign of the terms is given by the dot product and is not assumed a priori.

3. Results

3.1. Angle of attack sweep

This section presents the results obtained for TAU B/C powered simulations at increasing angle of attack covering the lift polar, focusing on the wing aerodynamics. The solutions were obtained starting from $\alpha = 6°$, which was then restarted to move towards higher incidence values by adding 3°, up to near stall at $\alpha = 18°$. This latter operating point is known to be challenging to reproduce with RANS modelling. Results from AIAA HLPW-4 [16] indicated a large spread among the participants at maximum C_L and suggested the use of very fine grids, with levels D or E. The purpose of analysing the near stall point here is not to provide a high-fidelity representation of the complex physics involved at this condition, but rather to illustrate the qualitative differences arising between models of comparable accuracy employing unpowered nacelles.

The surface flow is analysed in terms of pressure coefficient distribution and shear lines, which indicate the severity of suction peaks near the leading edges of the wing and high lift surfaces and the induced flow separation. Figs. 8 and 9 illustrate the wing and flap surface flow at $\alpha = 6°$, 12°, and 18°. Considering the top row only, showing the upper side, the flow field at 6° is characterised by a low suction peak with mild three-dimensional effects on the shear lines, apart from the area around the engine, where skin friction coefficient highlights the effect of vortices emitted by the nacelle chine and the slat cut. The flap suction side presents a clearly visible flow separation around the wing kink. At moderate incidence, spanwise flow components become stronger in the wing/fuselage junction, wing tip, and nacelle installation regions. The suction peak on the wing clearly increases with α, and the vortices forming in the slat cut-out and triggered by the nacelle chine leave a recognisable trace on the shear lines. The effect of the nacelle chine helps to mitigate the wing surface separation in the wing $C_{l,max}$ point at $\alpha = 18°$. However, the Spalart-Allmaras solution presents a large detached region in the wing tip, originating from a slat bracket and expanding downstream. Such feature has been already highlighted in Fig. 4, comparing wind tunnel and numerical data, and deviates from wind tunnel oil flow visualisation, which indicated a more distributed separation region near the wing tip, the stall being caused by a massive recirculation at the wing root.

Figs. 8 and 9 report the pressure side view on the bottom row. Here, skin friction lines illustrate a more three-dimensional flow having important spanwise components even at $\alpha = 6°$, especially in the mid-span area. Such feature is enhanced at higher incidence, with a noticeable separation line close to the leading edge. At $\alpha = 12°$ and 18°, the flow is driven towards the pylon from the outboard side and a separation zone is present at near stall, to the left of the pylon in Fig. 8c and 9c. The area of higher C_f and lower C_p indicates the noticeable effect caused by a vortex propagating from the wing/pylon junction and triggering the flow recirculation.

The vortices emanated from the leading edge cuts and chine are visualised by means of Q-criterion iso-structures in Fig. 10. A qualitative agreement with the analysis of [48] for the throughflow nacelle with chine is observed, in terms of flow structure and topology, with

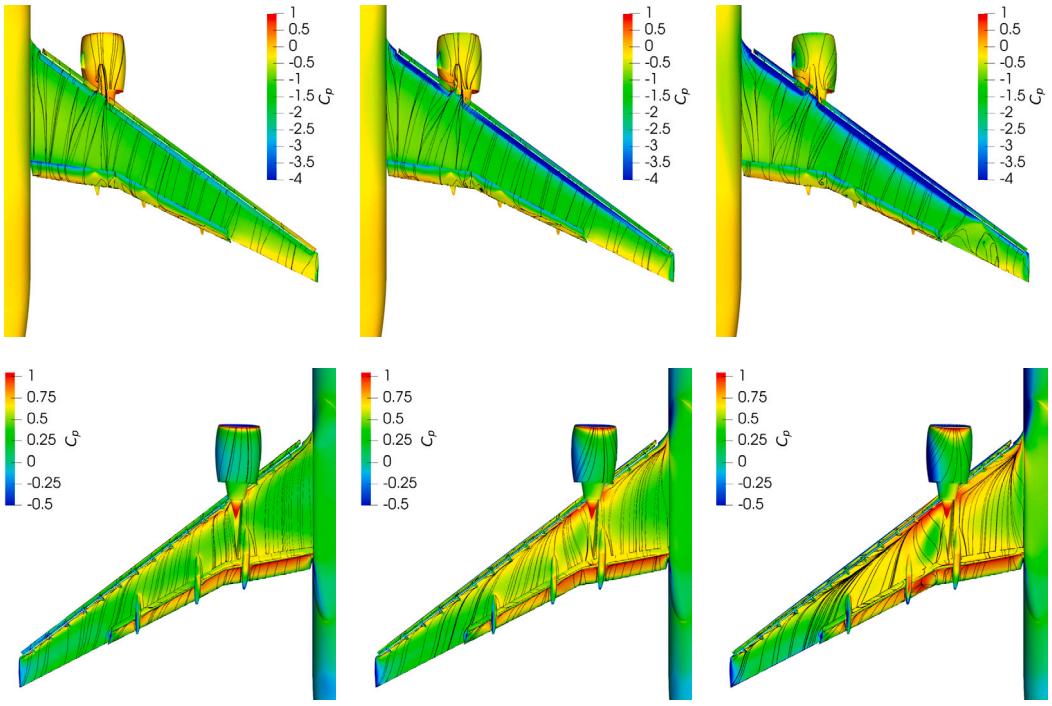

(a) $\alpha = 6°$ (b) $\alpha = 12°$ (c) $\alpha = 18°$

Fig. 8. Pressure coefficient distribution for TAU B/C powered simulations.

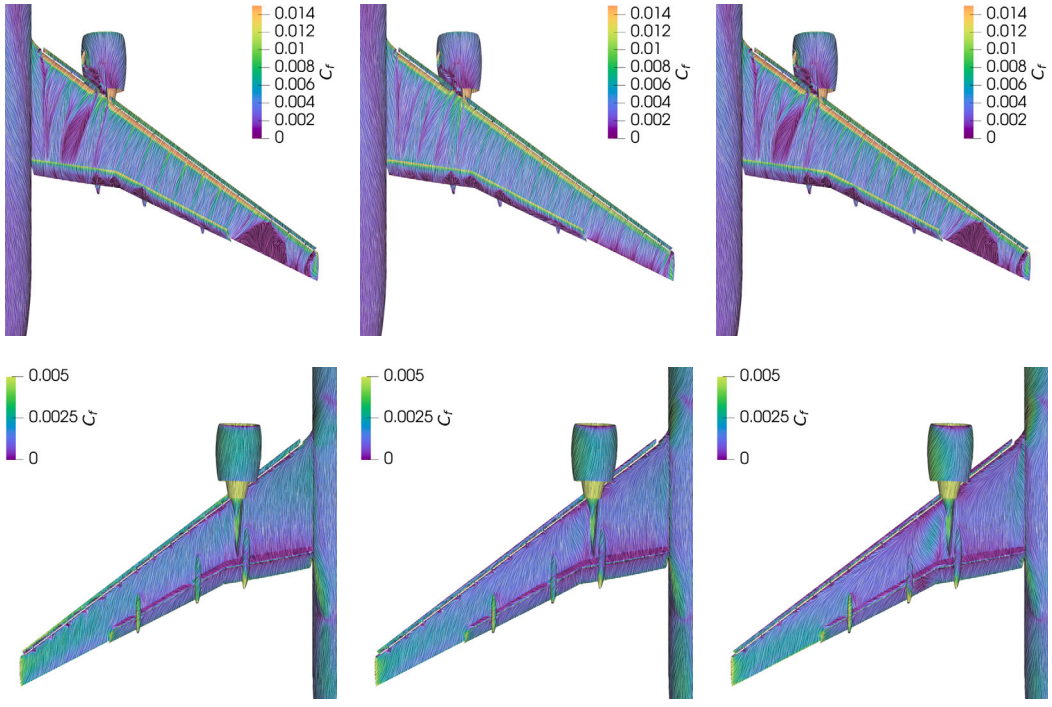

(a) $\alpha = 6°$ (b) $\alpha = 12°$ (c) $\alpha = 18°$

Fig. 9. Skin friction coefficient distribution for B/C powered simulations.

some differences in the nacelle/pylon area. A pair of vortices departs from the outboard slat and cut-out at all incidences. From the pylon and the nacelle, two distinct structures can be observed, one generating from the outboard side of the pylon, and one in the inboard side of the nacelle. The latter goes over the pylon and gets stronger passing through the wing intersection, eventually surmounting the former up to $\alpha = 12°$. At near stall, the nacelle vortices are deviated more inboard and they do not cross those coming from the pylon. The strongest structure originates from the nacelle chine and contributes to delaying the wing separation and ultimately the stall. Additional swirling patterns identified by the Q-criterion are those in the nacelle trailing edge and jet areas, but they do not interest the wing suction surface.

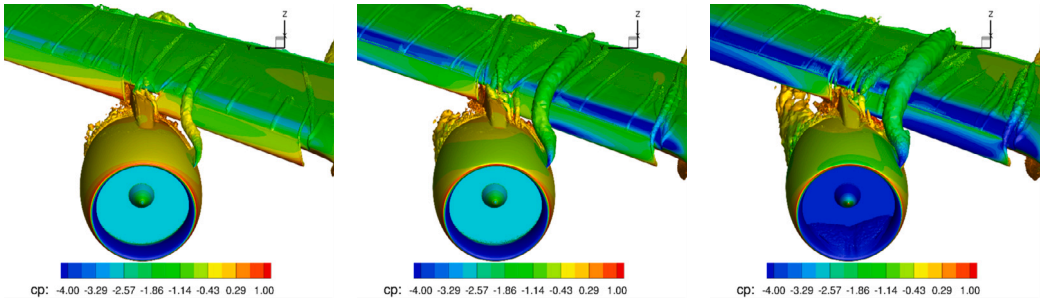

(a) $\alpha = 6°$ (b) $\alpha = 12°$ (c) $\alpha = 18°$

Fig. 10. Non dimensional Q-criterion iso-structures flooded by Cp contour.

3.2. Coupled fan/airframe simulations with BFM

3.2.1. Flow field

The results of the coupled fan/airframe simulations using the BFM model of the fan stage are here presented. As declared in Table 1, two angles of attack of 6° and 12° were investigated. The first aspect to be analysed is the pressure distribution on the nacelle external cowl surface. The installation, in fact, produces a highly three-dimensional flow, as shown before, associated to a large pressure field variation from the inboard to the outboard side and from the bottom to the top dead centre, due to the angle of attack. Fig. 11 presents three views, from the inboard, outboard, and top of the nacelle and pylon at the two incidence angles, together with friction lines that illustrate the wall shear. Due to the angle of attack, the pressure decreases from the bottom to the top dead centre close to the leading edge, as visible in Fig. 11a–11e. On the inboard side, the flow is diverted towards the top of the trailing edge and the shear lines released at the leading edge close to the keel diverge and migrate towards the pylon. This occurs similarly on the outboard side and the effect is magnified at the highest incidence. On the same side, the pylon presents a streamlined flow in the portion immersed in the fan stream, whereas the low-speed flow in the channel between the wing and the jet boundary separates from the pylon/wing joint leading edge. This separation is particularly visible inboard in Fig. 11a–11d. In this region, the flow is sensitive to the vortex emanated from the chine that passes over the upper part of the pylon and attaches to the wing. The effect of the chine is made even clearer in Fig. 11c–11f showing the view from the top, where the large vortical structure deviates the shear lines towards the pylon and generates a complex pressure trace on the walls. From the same figure, the inboard-to-outboard C_p variation can also be appreciated. The swept wing and the exposed high-lift surfaces induce a greater pressure on the inboard (top part in the figures) and a reduced pressure in the outboard. The difference enlarges at higher α and is equally present in the core cowl. The resulting force acting on the surfaces is thus significantly changed, compared to an isolated nacelle case, as explained later.

A further illustration of the installation effects is given in Fig. 12, where the axial C_p variation at different azimuthal angles on the nacelle external cowl and intake are compared for the same nacelle and pylon geometry simulated in isolation at equal flow model and boundary conditions. This second case is depicted with dashed lines in the figure. The four azimuthal positions are equispaced by 90° and the angle θ is defined in Fig. 12a, growing clockwise from the top dead centre when standing forward of the engine and looking aft. In the isolated model, the distribution on the two sides of the nacelle is the same, due to the symmetry of the geometry and the boundary conditions. For $\alpha = 6°$, the installed case shows a moderate difference between 45°–315° and 135°–225° in the intake suction peak and a larger variation on the external cowl, towards the trailing edge, as previously noticed. On the bottom half, the acceleration on the intake lip is larger than in isolation, indicating a locally higher incidence caused by wing upwash. Instead, the top half has a lower maximum M_{iso}. The 45° section is the one exhibiting the largest shift from the isolated case, especially at $\alpha = 12°$, where the external cowl is depressurised up to $x/c = 0.6$ and has a higher pressure from there onward, up to the trailing edge. At 135°, the pressure remains always higher than the uninstalled case, but the shift is rather constant. Noticeably, the suction peak is greatly enlarged, passing from $M_{iso} = 1.0$ for the isolated nacelle to $M_{iso} = 1.38$, which causes a shock wave to appear on the lip surface. The symmetric line on the outboard side, at 225°, has also a 15% larger M_{miso} on the intake, but the external cowl pressure is overlapped with the isolated nacelle.

The streamwise flow redistribution near the nacelle arising after powerplant integration is visualised in Fig. 13 on three vertical planes, one containing the engine axis and two located on opposite sides. The Mach number is illustrated along with the streamlines. The inboard plane is selected to cut the flap fairing in the middle, Fig. 13a–13d. The jet skims it in the current flap deflection and a large separation region is present above it. The flow field under the wing is similar for the two angles of attack, and it can be noticed that some flow is spilled from the nacelle trailing edge towards the wing. On the symmetry plane, Fig. 13b–13e, the streamlined pylon bottom surface opens up the core jet, that is driven upwards and further downstream is deviated back towards the engine axis by the flap wake. On the outboard plane, the difference between Fig. 13c and 13f is wider. The fan jet rotates more downward at $\alpha = 12°$, further pushed by the attached flow leaving the flap. The flow entering the channel between the nacelle and the wing is also more attracted towards the wing bottom surface.

The variability in the three pictures reveals important three-dimensional phenomena occurring, that need to be analysed also along the wingspan direction. Fig. 14 illustrates the Mach number distribution on three planes normal to the engine axis placed 2.8, 6.8, and 9.8 meters downstream of the fan nozzle exit section. In addition, the axial vorticity ω_x field lines are shown, allowing to superimpose it to the Mach number and appreciate the vortical structures developing in the planes. Closer to the bypass nozzle exit, Fig. 14a–14d, the jet boundary is well delineated. At $\alpha = 6°$, the field lines of ω_x are not completely radial, but rather straight, apart from the small region under the pylon. At 12°, small vortical structures appear on the outboard (right) portion of the fan stream, and on the wing upper side the strength of the swirling flows is larger. On plane 2, the jet remains symmetric at the lowest incidence, whereas the outboard lobe is more smeared at 12° and the vorticity lines indicate a stronger swirling core in that area. Here the nozzle stream passes close to the flap fairing and parts of the flow has been spilled towards the wing pressure side, as shown before. Farther from the nozzle, on plane 3, Fig. 14c–14f show that the highest angle of attack generates a large distortion of the plume cross section, with the outboard vortex in the right lobe pushing the jet towards the flap fairing. The interaction between the nozzle flow and the wing is thus clearly enhanced as the incidence grows and determines a significant redistribution of the engine jet.

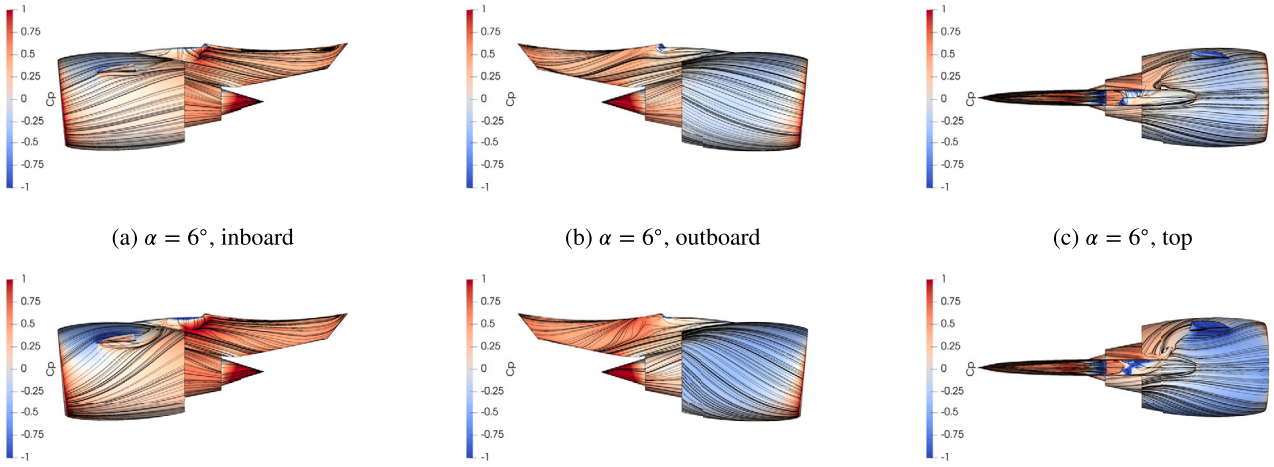

(a) $\alpha = 6°$, inboard (b) $\alpha = 6°$, outboard (c) $\alpha = 6°$, top

(d) $\alpha = 12°$, inboard (e) $\alpha = 12°$, outboard (f) $\alpha = 12°$, top

Fig. 11. Pressure coefficient distribution over the nacelle surface view from the inboard, outboard, and top with shear lines at $\alpha = 6°$ and 12°.

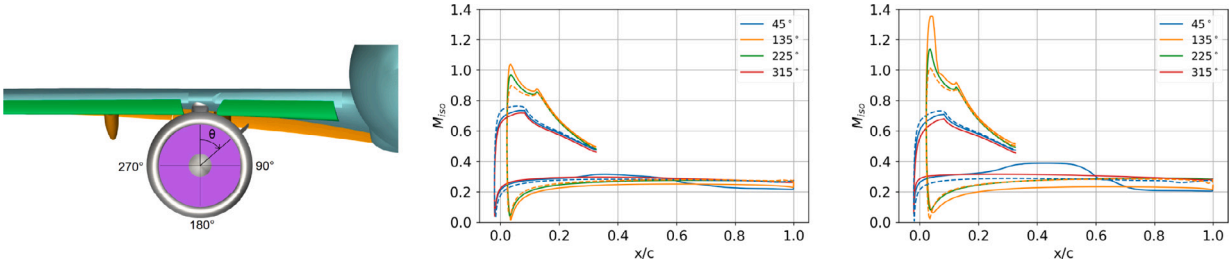

(a) Definition of the azimuthal angle θ (b) $\alpha = 6°$ (c) $\alpha = 12°$

Fig. 12. Isentropic Mach number distribution on nacelle external cowl and intake at different azimuthal locations. The azimuthal angle θ is defined in the first figure showing a forward looking aft view of the nacelle. Solid lines in the charts are for installed nacelle, dashed lines for isolated nacelle.

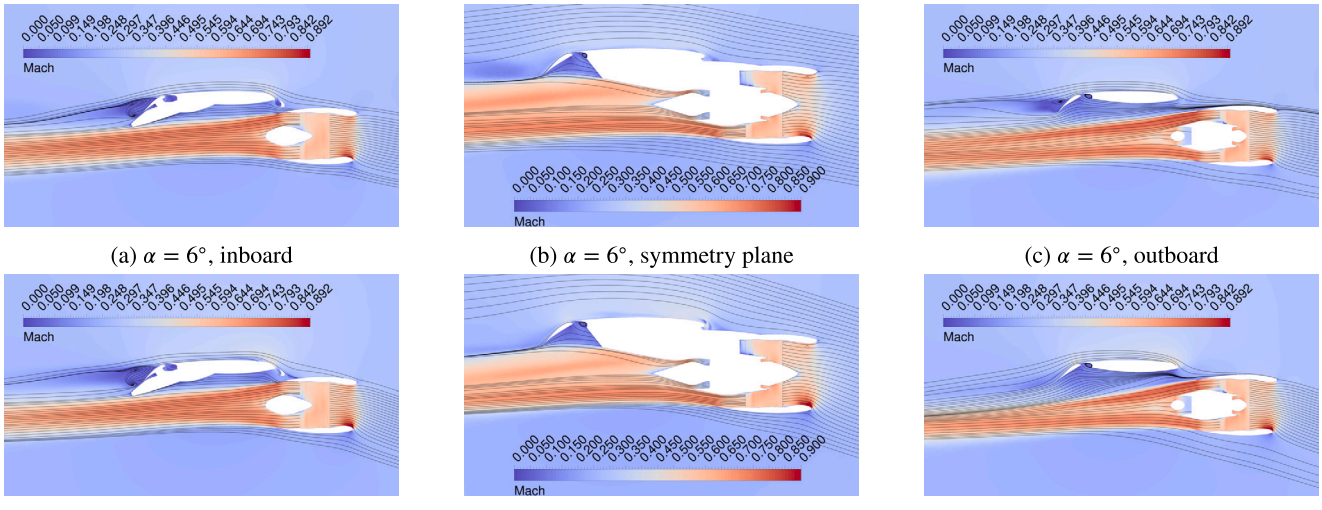

(a) $\alpha = 6°$, inboard (b) $\alpha = 6°$, symmetry plane (c) $\alpha = 6°$, outboard

(d) $\alpha = 12°$, inboard (e) $\alpha = 12°$, symmetry plane (f) $\alpha = 12°$, outboard

Fig. 13. Mach number distribution and streamlines on three vertical planes at $\alpha = 6°$ and 12°.

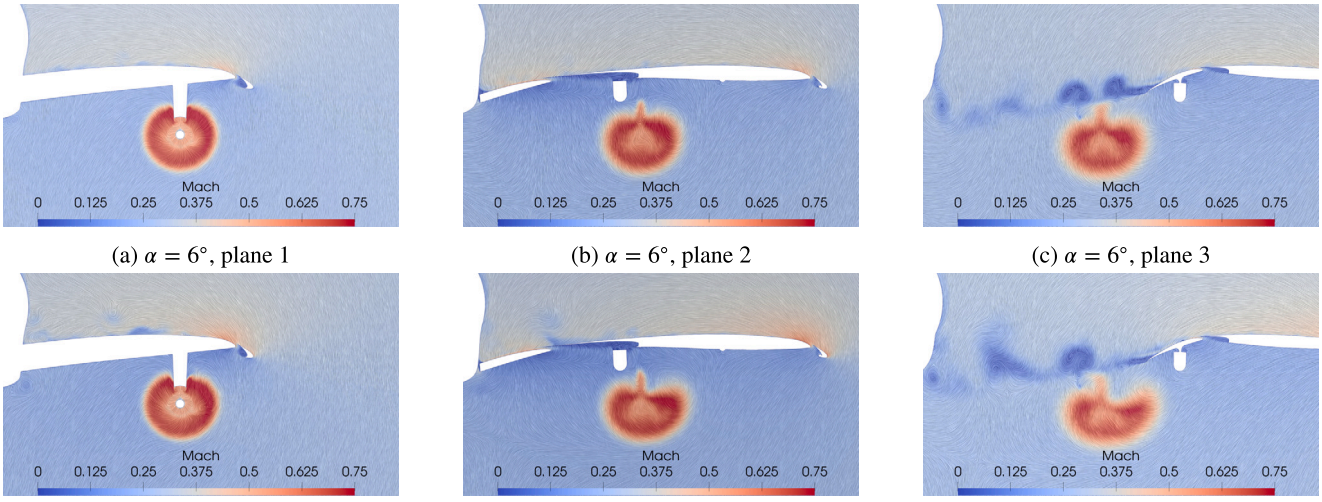

(a) $\alpha = 6°$, plane 1 (b) $\alpha = 6°$, plane 2 (c) $\alpha = 6°$, plane 3

(d) $\alpha = 12°$, plane 1 (e) $\alpha = 12°$, plane 2 (f) $\alpha = 12°$, plane 3

Fig. 14. Mach number distribution at different axial cross sections with field lines visualisation of axial vorticity at $\alpha = 6°$ and $12°$.

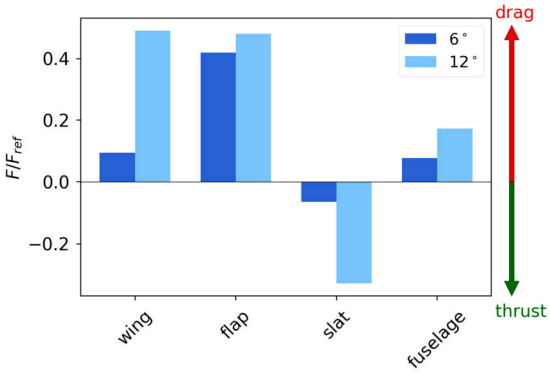

Fig. 15. Airframe drag force variation with angle of attack.

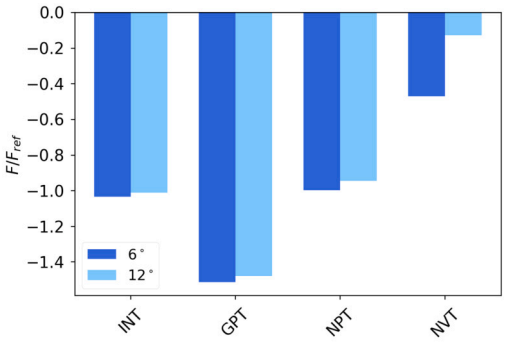

Fig. 16. Thrust variation with angle of attack.

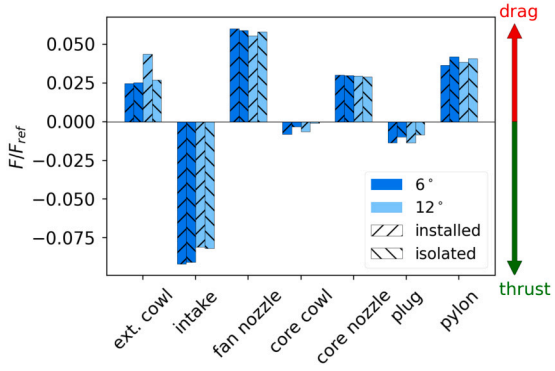

Fig. 17. Force distribution on nacelle surface for installed and isolated case.

3.2.2. *Propulsive forces*

After analysing the flow field, the propulsive forces acting on the UHBPR turbofan and the CRM-HL body are here investigated, according to the thrust/drag bookkeeping scheme defined in Sec. 2.3. The strong three-dimensional effects shown to arise under installation largely impact the pressure distribution, which dominates the resulting force, the viscous contribution being in general one to two order of magnitudes smaller.

The distribution of the drag force on the airframe is illustrated in Fig. 15. Values are normalised by a reference force amounting to the isolated engine axial gross thrust at zero incidence and equal flight conditions. The increase of the angle of attack produces a growth of the positive drag force on all surfaces apart from the slat. Here, a large negative thrust contribution appears, partially compensating the increase of airframe drag.

In terms of thrust, the situation is depicted in Fig. 16 according to the different definitions given. All normalised forces become less negative as α rises, with GPT, and NPT reducing in absolute value by 3.4% and 5.2%, relative to the reference force. The Net Vehicle Thrust NVT, representing the overall resulting force acting in the direction of flight, decreases by 34.2% in absolute value, as a consequence of the large drag rise.

In analysing the surface force contributions that bring to the shown drag and thrust distributions, it is interesting to compare it against the isolated nacelle case, to highlight the effect of the installation. Fig. 17 shows the wall forces acting on different nacelle parts. The major discrepancy occurs for the external cowl, that undergoes an increase of 1.9% from $\alpha = 6°$ to $12°$ under installation, because of the previously illustrated circumferential pressure variation and the separated areas caused by the chine vortex, not present in the isolated nacelle, where the force increment is ten times lower. Slightly differences are also present in the intake, but here the trend between the two configurations is the same, with a reduction of the lip thrust of 1.1%. Inside the two nozzle ducts, conversely, the increase of incidence attenuates the positive contribution to the drag, with a larger decrease, compared to the isolated case, in the fan nozzle. The exposed exhaust surfaces, instead, benefit from the wing pressure generating force component towards the thrust, more negative in the installed case thus. Finally, the pylon exhibits the same tendency, although the vortical structures re-

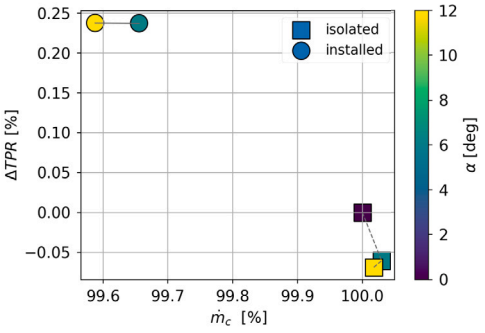

(a) Total Pressure Ratio

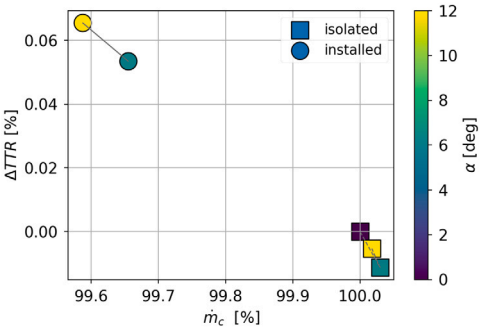

(b) Total Temperature Ratio

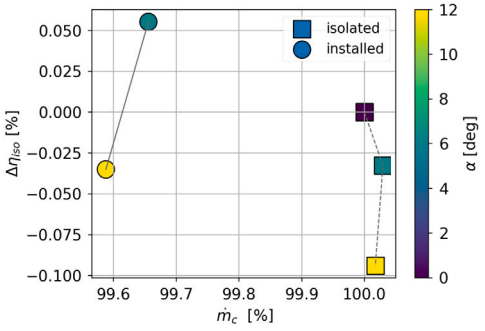

(c) Isentropic efficiency

Fig. 18. Characteristic maps of fan stage at increasing angle of attack for the isolated and installed engine.

duce the pressure in the front part giving a lower drag force in the mounted engine.

3.2.3. Fan operating conditions

The use of the BFM model for the fan representation offers the possibility to analyse, in addition to the aircraft aerodynamics, also the turbomachinery operating condition. The same model has been already employed to study fan/intake interaction up to large angles of attack, where separation develops, see for instance refs. [49,50]. Here, instead, the focus is on the effect of the underwing installation and in particular how it impacts the performance of the fan stage, compared to the isolated nacelle case at equal flight conditions.

The points on the characteristic map of the stage are illustrated in Fig. 18, where the ordinate reports the percentage shift of the corresponding variable from the reference condition, identified as the isolated nacelle at 0°, and the abscissa the percentage ratio of the corrected mass flow relative to the same reference condition. The data here described are clearly bounded to the accuracy of the adopted simplified blade model, which has some limitations in faithfully predicting the cascade behaviour far from the design condition [41]. However, the

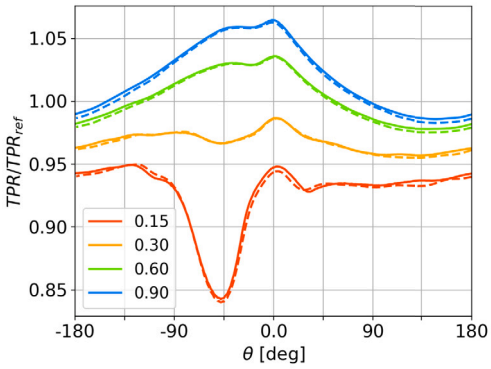

(a) $\alpha = 6°$

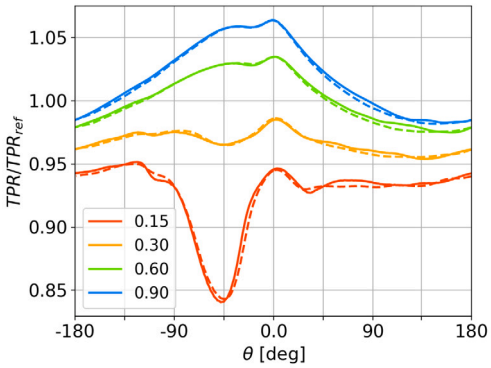

(b) $\alpha = 12°$

Fig. 19. Circumferential distribution of normalised total pressure ratio downstream of the fan stage for the isolated (dashed lines) and installed (solid lines) case.

model can provide at least a qualitative trend on how the stage reacts to the change of the boundary conditions, which is captured by body force methods [51]. In general, the angle of attack appears to have little influence in the simulated range, especially on the mass flow rate. Instead, the underwing installation alone determines a slight shift of the stage performance. For the Total Pressure Ratio (TPR), computed as the ratio between mass flow-averaged total pressure at the bypass nozzle inlet and at fan face, the installed case has 0.30% higher compression, relative to the isolated nacelle at the same angle of attack. This is in agreement with the clean characteristic, where TPR monotonically increases at lowering mass flow, up to the stall. The mild reduction of the mass flow can be attributed to the change of the discharge static pressure of the unchoked fan nozzle due to the wing and high-lift devices. A similar behaviour with very small variation is present in the Total Temperature Ratio (TTR), measuring the work input into the fluid, which is slightly more sensitive to α under installation. Finally, the adiabatic efficiency tends to dim as the incidence grows, with a moderate predicted jump less than 0.1% in the underwing-mounted configuration.

Fig. 19 depicts the circumferential distribution of TPR at the fan nozzle inlet at different span, comparing the isolated nacelle (dashed line) with the installed nacelle (solid line). Once again, the evolution is very close between the two cases, with small local differences but a limited influence of α. The specific distribution is driven by the strong effect of the pylon, blocking the flow at $\theta = 0°$ and pushing the local operating point towards higher work input and lower mass flux. This behaviour has already been analysed at cruise for the same configuration [29], is inherent to the engine integration into the present nacelle, and is dominant with respect to the influence of the inlet swirl and nozzle discharge conditions [50]. The TPR drop at 15% of span around $\theta = -45°$ is caused by a corner separation on the stator, owing to the ex-

cessive back-pressure due to potential interference as well. Overall, the impact of the wing installation on the fan operating conditions is thus estimated to be rather modest, despite the non-uniform pressure distribution outside the nozzle, visible in Fig. 11c–11f. A possible stronger effect might arise at larger angles of attack, where the fan is subject to inlet distortion and the outflow status might be more susceptible to the wing flow.

4. Conclusions

The NASA CRM-HL with underwing mounted powered UHBPR turbofan has been investigated along the wing polar and up to moderate incidence with a body force fan model. The aerodynamic analysis along the incidence sweep reveals that the flow structure and topology are qualitatively similar to those studied for the CRM-HL with throughflow nacelle at wind tunnel Reynolds number of 5.49M. In particular, the development of the flap suction surface separation, the vortex traces on the wing, and the flow recirculation at its root and tip appear analogous to the data reported in the literature. A more detailed analysis of the vortical structures emitted by the slat and wing cut-out, wing strake, nacelle, and pylon has confirmed such agreement, with minor differences in the vortices on the nacelle/pylon area. The flow on the wing pressure side, conversely, has been less investigated in the scope of the HLPW. The current study indicates a relevant effect of the pylon at near stall, with a separation line forming on the outboard side and a noticeable trace in pressure and skin friction coefficient caused by a swirling flow.

The effect of installation on the nacelle has been examined with a body force fan stage model at $\alpha = 6°$ and $\alpha = 12°$, further disclosing the complex three-dimensional flow that produces significant azimuthal variations, with a relevant upwash effect that aggravates the flow acceleration past the inlet lip, especially on the inboard side. The jet interaction with the pylon and wing is less severe than in high-speed cruise, where it triggers shock waves that alter the drag and lift, whereas at high incidence it skims the flap lower side and flap brackets without exhibiting discontinuities in the current case of an unchoked exhaust. Finally, the assessment of the fan operating point indicates a modest nozzle suppression on the mass flow rate and a consequent slight shift towards increased work input and compression, as long as no flow separation builds up in the inlet, like in the simulated scenario.

Overall, the study reveals the relevant aeropropulsive interaction occurring under installation at take-off, complementing previous research at cruise condition, and underlining the different complexity of this flow regime and the strong impact on the nacelle flow.

5. Funding

This study is financed by the Clean Sky 2 project IVANHOE (Installed adVAnced Nacelle uHbr Optimisation and Evaluation). The project has received funding from the European Union's Horizon 2020 research and innovation programme under grant agreement number 863415.

CRediT authorship contribution statement

Andrea Magrini: Investigation, Methodology, Software, Visualization, Writing – original draft, Writing – review & editing. **Gokul Subbian:** Investigation, Software, Validation, Visualization, Writing – review & editing. **Rolf Radespiel:** Conceptualization, Project administration, Supervision, Writing – review & editing. **Ernesto Benini:** Conceptualization, Project administration, Supervision, Writing – review & editing.

Declaration of competing interest

Andrea Magrini reports financial support was provided by Clean Sky Joint Technology Initiative.

Data availability

The authors do not have permission to share data.

Acknowledgement

The study was conducted within the PHD@UNIPD programme of the Foundation Cariparo under the project ANTENORE-Advanced iNvestigaTion at off-dEsigN Operation of uhbpR Engines.

The authors acknowledge University of Padova Strategic Research Infrastructure Grant 2017: "CAPRI: Calcolo ad Alte Prestazioni per la Ricerca e l'Innovazione" for providing computing infrastructure for numerical simulations.

References

[1] C. van Dam, The aerodynamic design of multi-element high-lift systems for transport airplanes, Prog. Aerosp. Sci. 38 (2) (2002) 101–144, https://doi.org/10.1016/S0376-0421(02)00002-7.

[2] C.L. Rumsey, S.X. Ying, Prediction of high lift: review of present CFD capability, Prog. Aerosp. Sci. 38 (2) (2002) 145–180, https://doi.org/10.1016/S0376-0421(02)00003-9.

[3] C.L. Rumsey, J.P. Slotnick, M. Long, R.A. Stuever, T.R. Wayman, Summary of the first AIAA CFD high-lift prediction workshop, J. Aircr. 48 (6) (2011) 2068–2079, https://doi.org/10.2514/1.C031447.

[4] C.L. Rumsey, J.P. Slotnick, Overview and summary of the second AIAA high-lift prediction workshop, J. Aircr. 52 (4) (2015) 1006–1025, https://doi.org/10.2514/1.C032864.

[5] C.L. Rumsey, J.P. Slotnick, A.J. Sclafani, Overview and summary of the third AIAA high lift prediction workshop, J. Aircr. 56 (2) (2019) 621–644, https://doi.org/10.2514/1.C034940.

[6] C.L. Rumsey, J.P. Slotnick, C.D. Woeber, Fourth high-lift prediction/third geometry and mesh generation workshops: overview and summary, J. Aircr. 60 (4) (2023) 1160–1177, https://doi.org/10.2514/1.C037168.

[7] Y. Yokokawa, M. Murayama, M. Kanazaki, K. Murota, T. Ito, K. Yamamoto, Investigation and improvement of high-lift aerodynamic performances in lowspeed wind tunnel testing, in: 46th AIAA Aerospace Sciences Meeting and Exhibit, AIAA, Reston, VA, 2008.

[8] D.S. Lacy, A.J. Sclafani, Development of the high lift common research model (HL-CRM): a representative high lift configuration for transonic transports, in: 54th AIAA Aerospace Sciences Meeting, AIAA, 2016.

[9] K. Zore, S. Shah, J. Stokes, B. Sasanapuri, P. Sharkey, ANSYS CFD study for high lift aircraft configurations, in: 2018 Applied Aerodynamics Conference, AIAA, Reston, VA, 2018.

[10] R. Rudnik, S. Melber-Wilkending, P. Risley-Settle, Tau-solar contributions to the 3rd high lift prediction workshop, in: 2018 AIAA Aerospace Sciences Meeting, AIAA, Reston, VA, 2018.

[11] J.C. Duensing, J.A. Housman, L. Fernandes, L. Machado, C.C. Kiris, A Reynolds-averaged Navier-Stokes perspective for the high lift-common research model using the LAVA framework, in: AIAA Aviation 2022 Forum, AIAA, Reston, VA, 2022.

[12] N.N. Ahmad, L. Wang, W.K. Anderson, P. Balakumar, P.S. Iyer, E.J. Nielsen, FUN3D simulations for the 4th AIAA high-lift prediction workshop, in: AIAA Aviation 2022 Forum, AIAA, Reston, VA, 2022.

[13] P. Li, J. Gallegos, T.R. Michal, Generation of mixed element unstructured meshes for the 3rd high lift prediction workshop, in: 55th AIAA Aerospace Sciences Meeting, AIAA, Reston, VA, 2017.

[14] C.D. Woeber, E.J. Gantt, N.J. Wyman, Mesh generation for the NASA high lift common research model (HL-CRM), in: 55th AIAA Aerospace Sciences Meeting, AIAA, Reston, VA, 2017.

[15] W.T. Jones, C. Woeber, A qualitative study on the effects of mesh guideline modification for unstructured mesh generation of the NASA high lift common research model (HL-CRM), in: 2018 Fluid Dynamics Conference, AIAA, Reston, VA, 2018.

[16] C.F.O. Gooch, J.G. Coder, Lessons learned by the fixed-grid RANS TFG for HLPW-4/GMGW-3, in: AIAA Aviation 2022 Forum, AIAA, Reston, VA, 2022.

[17] M. Koklu, L.G.P. Melton, J.C. Lin, J. Hannon, M. Andino, K. Paschal, V.N. Vatsa, Surface flow visualization of the high lift common research model, in: AIAA Aviation 2019 Forum, AIAA, Reston, VA, 2019.

[18] M.A. Park, F. Alauzet, T. Michal, HLPW-4/GMGW-3: mesh adaptation for RANS technology focus group workshop summary, J. Aircr. 60 (4) (2023) 1219–1237, https://doi.org/10.2514/1.C037192.

[19] M.C. Galbraith, S.L. Karman, HLPW-4/GMGW-3: high-order discretization technology focus group workshop summary, J. Aircr. 60 (5) (2023) 1613–1625, https://doi.org/10.2514/1.C037181.

[20] C.C. Kiris, A.S. Ghate, O.M. Browne, J.P. Slotnick, J. Larsson, HLPW-4/GMGW-3: wall-modeled LES and Lattice-Boltzmann technology focus group workshop summary, in: AIAA Aviation 2022 Forum, AIAA, Reston, VA, 2022.

[21] European Commission, FlightPath 2050, Tech. rep., ACARE, Luxembourg, 2011, https://ec.europa.eu/transport/sites/transport/files/modes/air/doc/flightpath2050.pdf.
[22] F. Afonso, M. Sohst, C.M. Diogo, S.S. Rodrigues, A. Ferreira, I. Ribeiro, R. Marques, F.F. Rego, A. Sohouli, J. Portugal-Pereira, H. Policarpo, B. Soares, B. Ferreira, E.C. Fernandes, F. Lau, A. Suleman, Strategies towards a more sustainable aviation: a systematic review, Prog. Aerosp. Sci. 137 (2023) 100878, https://doi.org/10.1016/j.paerosci.2022.100878.
[23] P.D. Bravo-Mosquera, F.M. Catalano, D.W. Zingg, Unconventional aircraft for civil aviation: a review of concepts and design methodologies, Prog. Aerosp. Sci. 131 (2022) 100813, https://doi.org/10.1016/j.paerosci.2022.100813.
[24] A. Magrini, E. Benini, H.-D. Yao, J. Postma, C. Sheaf, A review of installation effects of ultra-high bypass ratio engines, Prog. Aerosp. Sci. 119 (2020) 100680, https://doi.org/10.1016/j.paerosci.2020.100680.
[25] S. Salehian, R. Mankbadi, Jet noise in airframe integration and shielding, Appl. Sci. 10 (2) (2020), https://doi.org/10.3390/app10020511.
[26] C. Jente, M. Pott-Pollenske, D. Boenke, A. Buescher, I. Goldhahn, Experimental investigation of jet-flap-interaction noise sensitivity due to varying flap parameters at a UHBR engine/high-lift-wing installation, in: 2018 AIAA/CEAS Aeroacoustics Conference, AIAA, Reston, VA, 2018.
[27] M. Angelino, M.A. Moratilla-Vega, A. Howlett, H. Xia, G.J. Page, Numerical investigation of installed jet noise sensitivity to lift and wing/engine positioning, in: 25th AIAA/CEAS Aeroacoustics Conference, AIAA, Reston, VA, 2019.
[28] C. Teruna, L. Rego, D. Casalino, D. Ragni, F. Avallone, A numerical study on aircraft noise mitigation using porous stator concepts, Aerospace 9 (2) (2022), https://doi.org/10.3390/aerospace9020070.
[29] A. Magrini, E. Benini, Aeropropulsive assessment of engine installation at cruise for UHBPR turbofan with body force fan modelling, Aerosp. Sci. Technol. 132 (2023) 108048, https://doi.org/10.1016/j.ast.2022.108048.
[30] D.S. Lacy, A.M. Clark, Definition of initial landing and takeoff reference configurations for the high lift common research model (CRM-HL), in: AIAA, 2020.
[31] A. Magrini, D. Buosi, E. Benini, Analysis of installation aerodynamics and comparison of optimised configuration of an ultra-high bypass ratio turbofan nacelle, Aerosp. Sci. Technol. 128 (2022) 107756, https://doi.org/10.1016/j.ast.2022.107756.
[32] A. Magrini, D. Buosi, E. Benini, Maximisation of installed net resulting force through multi-level optimisation of an ultra-high bypass ratio engine nacelle, Aerosp. Sci. Technol. 119 (2021) 107169, https://doi.org/10.1016/j.ast.2021.107169.
[33] A. Magrini, D. Buosi, E. Benini, C. Sheaf, Ultra-high bypass nacelle geometry design space exploration, in: AIAA Scitech 2021 Forum, AIAA, Reston, VA, 2021.
[34] E. Goldsmith, J. Seddon, Practical Intake Aerodynamic Design, AIAA Education Series, American Institute of Aeronautics and Astronautics, 1993, https://books.google.it/books?id=8-tGAQAAIAAJ.
[35] D.L. Motycka, Reynolds number and fan/inlet coupling effects on subsonic transportinlet distortion, J. Propuls. Power 1 (3) (1985) 229–234, https://doi.org/10.2514/3.22785.
[36] A.N. Evans, D.S. Lacy, I. Smith, M.B. Rivers, Test summary of the NASA high-lift common research model half-span at QinetiQ 5-metre pressurized low-speed wind tunnel, in: AIAA Aviation 2020 Forum, AIAA, 2020.
[37] D. Schwamborn, T. Gerhold, R. Heinrich, The DLR TAU-code: recent applications in research and industry, in: ECCOMAS CFD 2006 Conference, DLR, 2006, https://elib.dlr.de/22421/.
[38] S.R. Allmaras, F.T. Johnson, P.R. Spalart, Modifications and clarications for the implementation of the Spalart-Allmaras turbulence model, in: International Conference on Computational Fluid Dynamics, ICCFD7, 2012.
[39] O.M.F. Browne, J.A. Housman, G.K. Kenway, A.S. Ghate, C.C. Kiris, Numerical investigation of CL,max prediction on the NASA high-lift common research model, AIAA J. 61 (4) (2023) 1639–1658, https://doi.org/10.2514/1.J062508.
[40] W. Thollet, G. Dufour, X. Carbonneau, F. Blanc, Body-force modeling for aerodynamic analysis of air intake – fan interactions, Int. J. Numer. Methods Heat Fluid Flow 26 (7) (2016) 2048–2065.
[41] A. Magrini, Body force model implementation of transonic rotor for fan/airframe simulations, Aerospace 9 (11) (2022), https://doi.org/10.3390/aerospace9110725.
[42] B. Mohankumar, C.A. Hall, M.J. Wilson, Fan aerodynamics with a short intake at high angle of attack, J. Turbomach. 143 (5 2021), https://doi.org/10.1115/1.4050606.
[43] ANSYS, ANSYS Fluent 19.2 Theory Guide, ANSYS, Inc., 2018.
[44] F. Menter, Improved two-equation k-omega turbulence models for aerodynamic flows, Technical Memorandum 19930013620, NASA, https://ntrs.nasa.gov/citations/19930013620, 1992.
[45] M. Zastawny, J. Hanke, C.C. Nelson, Fixed grid RANS results and turbulence model investigation using simcenter STAR-CCM+ for 4th AIAA CFD high lift prediction workshop, in: AIAA Aviation 2022 Forum, AIAA, Reston, VA, 2017.
[46] G. Subbian, A. Magrini, D. Buosi, R. Radespiel, R. Ponza, E. Benini, Investigation of HL-CRM aerodynamics with a UHBPR nacelle in powered-on condition, in: AIAA Propulsion and Energy 2021 Forum, AIAA, Reston, VA, 2021.
[47] G. Subbian, A. Magrini, E. Benini, D. Buosi, R. Ponza, R. Radespiel, Rans analysis of HL-CRM at take-off and landing configurations with different flap deflections and engine settings using DLR-TAU code, in: AIAA Scitech 2021 Forum, AIAA, Reston, VA, 2022.
[48] M. Koklu, J.C. Lin, J.A. Hannon, L.P. Melton, M.Y. Andino, K.B. Paschal, V.N. Vatsa, Investigation of the nacelle/pylon vortex system on the high-lift common research model, AIAA J. 59 (9) (2021) 3748–3763, https://doi.org/10.2514/1.J059869.
[49] A. Magrini, E. Benini, Study of geometric parameters for the design of short intakes with fan modelling, Chin. J. Aeronaut. 35 (11) (2022) 18–32, https://doi.org/10.1016/j.cja.2022.01.018.
[50] A. Magrini, D. Bousi, E. Benini, Analysis of ultra-high bypass ratio turbofan nacelle geometries with conventional and short intakes at take-off and cruise, in: Volume 10C: Turbomachinery — Design Methods and CFD Modeling for Turbomachinery; Ducts, Noise, and Component Interactions of Turbo Expo: Power for Land, Sea, and Air, ASME, New York, NY, 2022.
[51] D.K. Hall, E.M. Greitzer, C.S. Tan, Analysis of fan stage conceptual design attributes for boundary layer ingestion, J. Turbomach. 139 (7) (Jul. 2017), https://doi.org/10.1115/1.4035631.